ACS APPLIED MATERIALS & INTERFACES

Research Article

www.acsami.org

Core-shell Structured Hyperbranched Aromatic Polyamide/$BaTiO_3$ Hybrid Filler for Poly(vinylidene fluoride-trifluoroethylene-chlorofluoroethylene) Nanocomposites with the Dielectric Constant Comparable to That of Percolative Composites

Liyuan Xie, Xingyi Huang,* Yanhui Huang, Ke Yang, and Pingkai Jiang*

Department of Polymer Science and Engineering and Shanghai Key Laboratory of Electrical Insulation and Thermal Aging, Shanghai Jiao Tong University, Shanghai 200240, People's Republic of China

ABSTRACT: Polymer nanocomposites with the dielectric constant comparable to that of percolative composites are successfully prepared by using core−shell structured hyperbranched aromatic polyamide grafted barium titanate (BT-HBP) hybrid nanofiller. Poly(vinylidene fluoride-trifluoroethylene-chlorofluoroethylene) (PVDF-TrFE-CFE) was used as the polymer matrix because of its high intrinsic dielectric constant and easy processability. The BT-HBP hybrid nanofiller were prepared by a solution polymerization of diaminobenzoic acid on the surface of amino-funcationalized BT nanoparticles. Nuclear magnetic resonance (^{1}H NMR) and transmission electron microscopy (TEM) were used to verify the chemical structure of the hyperbranched aromatic polyamide and core-shell structure of the hybrid filler, respectively. It was found that the nanocomposite with 40 vol % $BaTiO_3$−HBP had a dielectric constant of 1485.5 at 1000 Hz, whereas the corresponding nanocomposite sample with untreated $BaTiO_3$ only showed a dielectric constant of 206.3. Compared with classic percolative composites, the advantage of the PVDF-TrFE-CFE/$BaTiO_3$−HBP nanocomposites is that the composites show high enough breakdown strength and high dielectric constant simultaneously. An enhanced interfacial polarization mechanism between the BT-HBP and the polymer matrix was suggested for understanding the observed unusually high dielectric constant.

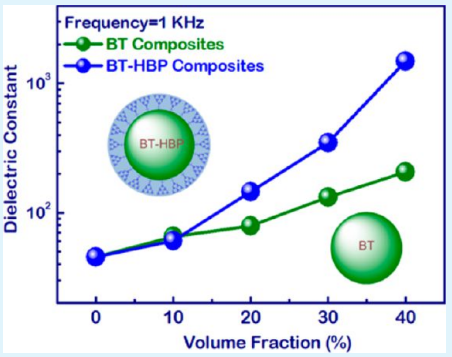

KEYWORDS: *high dielectric constant, core−shell structure, poly (vinylidene fluoride-trifluoroethylene-chlorofluoroethylene), barium titanate nanoparticles, interfacial polarization*

1. INTRODUCTION

Dielectric materials with high dielectric constant have a variety of applications in capacitors,[1,2] gate dielectrics,[3] actuators[4,5] and electric stress control.[6] Because of the ease of processability and low cost, polymer-based materials with high dielectric constant become more and more important for dielectric applications. Most of pure polymers for dielectric applications have low dielectric constant (e.g, <10); therefore, current studies have focused on the fabrication of high dielectric constant polymer composites.[7,8] So far several methods have been developed to prepare polymer composites with high dielectric constant. One classic approach is to introduce high dielectric constant ceramic nanoparticles (e.g., $BaTiO_3$[9−12]) into a polymer. The advantage of this method is that the dielectric constant of ceramic polymer nanocomposites can be well controlled by adjusting the ceramic particle loading. Moreover, the corresponding nanocomposites also usually possess relative high dielectric strength and low dielectric loss. However, the dielectric constant enhancement in the composites is limited and the enhancement factor is usually less than 10 even the filler loading is as high as 60 vol %.[13]

Preparing percolative composites, namely dispersing conductive fillers such as metal particles,[14,15] carbon nanotubes,[16,17] graphene,[18−20] conductive oxide,[21] and conductive polymers[22,23] into a polymer, has also been widely utilized to realize high dielectric constant. The advantage of this approach is that the dielectric constant of the percolative composites increases dramatically when the volume fraction of filler increases to the vicinity of the percolation threshold.[24] However, this kind of composites suffers from high dielectric loss and very low breakdown strength. Moreover, it is difficult to control the dielectric constant by adjusting the filler loading because that, in the vicinity of percolation threshold, a small difference in filler loading could cause great variation in dielectric constant of the composites.[25] Overall, the preparation of high-performance polymer nanocomposite with significantly increased dielectric constant is still a great challenge.

Taking the aforementioned content into account, it is highly desirable to prepare dielectric ceramic filler-based polymer nanocomposites having dielectric constant comparable to that of percolative composites. Herein, we report a strategy to prepare such a type of polymer nanocomposite. Hyperbranched

Received: December 4, 2012
Accepted: February 4, 2013
Published: February 4, 2013

   dx.doi.org/10.1021/am302959n | ACS Appl. Mater. Interfaces 2013, 5, 1747−1756

aromatic polyamide encapsulated $BaTiO_3$ nanoparticles and poly (vinylidene fluoride-trifluoroethylene-chlorofluoroethylene) (PVDF-TrFE-CFE) were used as high dielectric constant fillers and polymer matrix, respectively. The results show that the nanocomposites exhibit high enough breakdown strength and high dielectric constant simultaneously.

2. EXPERIMENTAL SECTION

2.1. Materials. The $BaTiO_3$ (BT) nanoparticles with an average diameter of 100 nm were obtained from the Shandong Sinocera Functional Material Company, China. γ-Aminopropyl triethoxysilane (γ-APS) purchased from GE silicones was used as a coupling agent. The grafting monomer 3,5-diaminobenzoic acid (DABA) was supplied by Tokyo Chemical Industry Co. Ltd., Japan. DABA was recrystallized from hot water and dried in a vacuum at 80 °C for 12 h before use. Lithium chloride (LiCl, Shanghai Reagents Co. Ltd.) was dried at 230 °C overnight before use. Aqueous solution of H_2O_2 (30 wt %), triphenyl phosphite (TPP), N-methyl-2-pyrrolidone (NMP), N,N-dimethyl formamide (DMF), methanol, toluene, pyridine, and other chemicals were supplied by Shanghai Reagents Co. Ltd. PVDF-TrFE-CFE was supplied from PiezoTech, France. Unless otherwise specified, all the chemicals were used as-received.

2.2. Preparation of Core−Shell Structured BT Nanoparticles. Three steps were used to prepare hyperbranched aromatic polyamide grafted BT (BT-HBP) nanoparticles:

Step 1. Hydroxylation of as received BT nanoparticles: 15 g of BT nanoparticles were added into 80 mL of an aqueous solution of H_2O_2 (30 wt %) in a round-bottomed flask. The mixture was sonicated for 30 min (250 W) and then was refluxed at 105 °C for 4 h. The nanoparticles were recovered by centrifugation at 9000 rpm for 5 min. The obtained BT nanoparticles were washed with deionized water two times and then were dried under vacuum at 80 °C for 12 h. The hydroxylated BT nanoparticles were named as BT-OH.

Step 2. Functionalization of BT-OH by amino groups: 10 g of BT-OH nanoparticles were first added into 80 mL of toluene in a round-bottomed flask and sonicated for 30 min, and then 5 g γ-APS was added and the mixture was heated to 80 °C for 24 h under a N_2 atmosphere. The nanoparticles were recovered by centrifugation at 9000 rpm for 5 min. The obtained nanoparticles were washed with toluene two times and were dried under vacuum at 80 °C for 12 h and named as BT-APS. Toluene was chosen as the solvent for silanization is because that, under anhydrous conditions, the silane molecules tend to form monolayer on the surface of inorganic fillers.

Step 3. Grafting of hyperbranched aromatic polyamide onto the surface of BT-APS. In a flask, 2 g of γ-APS treated BT (BT-APS) was added into 20 mL of NMP and the mixture was sonicated for 30 min to disperse the BT-APS. 2 g DABA was added into the mixture and stirred until the DABA was dissolved. Then 5 ml pyridine, 5 mL TPP and 0.042 LiCl were added. The mixture was heated to 100 °C and stirred under nitrogen for 3 h. when the temperature decreased to room temperature, the mixture was poured into 50 mL of methanol containing 0.1% LiCl to remove the unreacted monomer DABA. The precipitated BT nanoparticles and hyperbranched aromatic polyamide were redissolve in DMF and centrifuged at 9000 rpm for 5 min to remove pure hyperbranched aromatic polyamide. The obtained BT nanoparticles were dried under vacuum at 80 °C for 12 h and denoted as BT-HBP.

3.3. Preparation of BT Nanocomposites. The nanocomposites were prepared via a solution blending method. First, the required quantity of nanoparticles was dispersed into DMF under 30 min sonication at room temperature. At the same time, PVDF-TrFE-CFE was dissolved in DMF at 80 °C. The suspension of DMF and nanoparticles were then mixed with the solution of PVDF-TrFE-CFE/DMF solution with an electric stirrer at 80 °C for 30 min. The resulting mixture was dried on a hot plate at 120 °C and then under vacuum at 80 °C for 12 h. Finally, the dried nanocomposites were compressed into films at 180 °C under a pressure of about 20 MPa. For the sake of comparison, the nanocomposites were denoted as particle type-volume fraction. For example, BT-30 and BT-HBP-30 indicate the nanocomposites with 30 vol% as received BT and BT-HBP, respectively.

3.4. Characterization. Fourier-transform infrared spectroscopy (FTIR) was conducted with a Perkin-Elmer Paragon 1000 instrument over the range of 4000-450 cm^{-1}. Nuclear magnetic resonance (^1H NMR) spectra was recorded with a Varian Mercury plus-400 spectrometer in DMSO-d_6, using TMS as the standard. Thermogravimetric analysis (TGA) was conducted using a NETZSCH TG209 F3 instrument with a heating rate of 20 °C min^{-1} in an air flow (20 ml min^{-1}). Dynamic light scattering measurement was conducted using a Nano-ZS90 ZetaSizer instrument (Malvern Instruments Ltd., UK). All the particles were dispersed in DMF by sonication. X-ray photoelectron spectroscopy (XPS) was recorded with an Axis Ultra spectrometer (Kratos Analytical, UK) with a monochromated Al Kα source. Survey scans over a binding energy range of 0 - 1150 eV were taken for each sample with a constant detector pass energy range of 160 eV, followed by high-resolution XPS measurement (pass energy 40 eV) for quantitative measurements of binding energy and atomic concentration. Transmission electron microscopy (TEM) images were obtained from a JEOL JEM-2100 instrument operated at an accelerating voltage at 160 kV. Samples were prepared by dropping the sample solutions onto carbon-coated copper grids and air-dried before measurement. Scanning electron microscopy (SEM) images were recorded using a JEOL JEM 7401F field-emission scanning electron microscope. All samples were prepared by fracturing the composites at liquid nitrogen temperature and then sputter-coated with a homogeneous gold layer to avoid accumulation of charges. The broadband frequency dielectric properties of the composites were measured using a Solartron SI 1260 impedance analyzer (Advanced Measurement Technology, Inc., U.K.) in a frequency range of 1×10^{-1} to 1×10^6 Hz at various temperatures. All of the samples had a layer of gold evaporated on both surfaces to serve as electrodes. The DC breakdown strength was measured by a dielectric strength tester (DH, Shanghai Lanpotronics Co., China).

3. RESULTS AND DISCUSSION

3.1. Preparation and Characterization of BT-HBP. Scheme 1 shows the synthesis of core-shell structured BT-HBP hybrid filler. For the functionalization of inorganic nanoparticles, hydroxyl (−OH) groups are important bridges for the introduction of other functional groups. The as received BT nanoparticles have small amounts of −OH groups on their surfaces and thus the first step for the functionalization of BT nanoparticles is to introduce −OH groups by refluxing the

Scheme 1. Schematic Diagram Illustrating the Preparing Process of BT-HBP

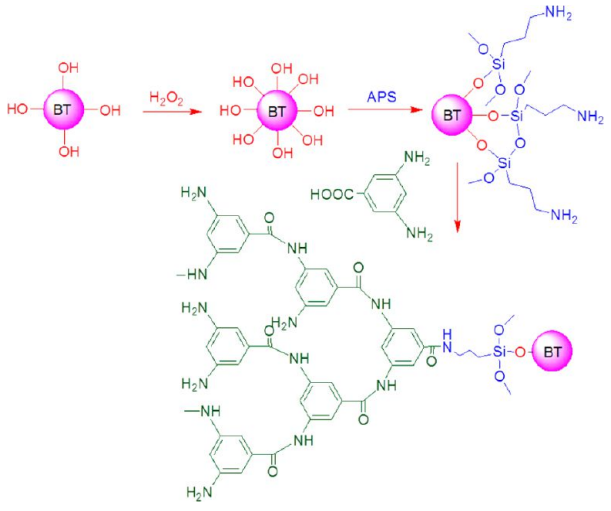

nanoparticles in H_2O_2 aqueous solution.[26,27] Then the hydroxylated BT (BT-OH) nanoparticles were reacted with γ-APS in anhydrous toluene, forming γ-APS functionalized BT nanoparticles (BT-APS). Figure 1 shows the FTIR spectra of

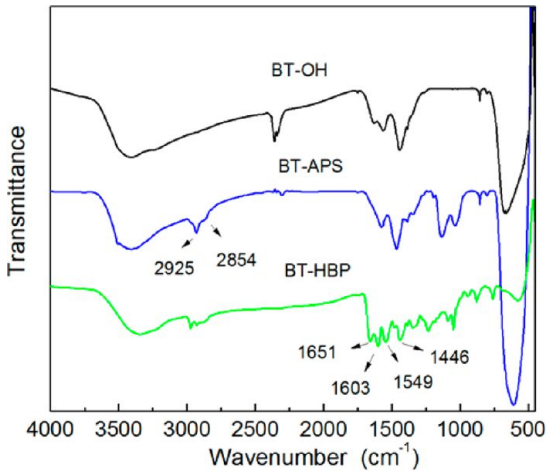

Figure 1. FT-IR spectra of BT-OH, BT-APS, and BT-HBP.

BT-APS nanoparticles. The appearance of 2925 and 2854 cm^{-1} absorption peaks, which are attributed to the asymmetric and symmetric $-CH_2$ stretching vibrations, indicates that γ-APS has been successfully introduced onto the surface of BT nanoparticles.

The final step for preparing BT-HBP is to grow a layer of hyperbranched aromatic polyamide on the surface of the BT nanoparticles. Hyperbranched aromatic polyamide is highly branched macromolecule with three-dimensional spherical architecture and is considered as a fine coating agent of nanoparticles.[28−30] It can be prepared by either homo- or copolymerization of ABx building blocks or by copolymerization of Ax and By type monomers.[31] In this contribution, direct polycondensation of 3, 5-diaminobenzoic acid was employed. Triphenyl phosphite (TPP) and pyridine were used as condensing agents (Yamazaki reaction); LiCl was used as solubility promoter because the cations interact with the amide groups, diminishing the strength of the interchain hydrogen bonds.[32] The FTIR spectra of BT-HBP nanoparticles are also shown in Figure 1. The broad absorption bands in the range of 3500−3000 cm^{-1} are assigned to the N−H stretching of amide group and the C−H stretching of benzene rings. The peaks at 1651 and 1549 cm^{-1} can be attributed to amide C═O stretching and the peaks at 1603 and 1446 cm^{-1} are characteristics of aromatic structure. These changes of FTIR spectra indicate that the hyperbranched aromatic polyamides have been grafted successfully onto the surfaces of the BT-APS nanoparticles.

The ^{1}H-NMR spectra of BT-HBP nanoparticles provides more detailed evidence to prove the successful introduction of hyperbranched aromatic polyamides onto the surface of BT nanoparticles. As can be seen in Figure 2, the ^{1}H-NMR spectra clearly display the characteristic peaks from the aromatic protons.[28,33] For example, the peaks at 8.3 and 7.9 ppm are attributed to the aromatic protons of the dendritic units, whereas the peaks at 7.3 and 6.8 ppm and those at 6.3 and 6.0 ppm are ascribed to those of the linear and terminal units, respectively. In addition, the amide groups at 10.6−9.8 ppm are also observed. The signal of the characteristic peaks is relatively

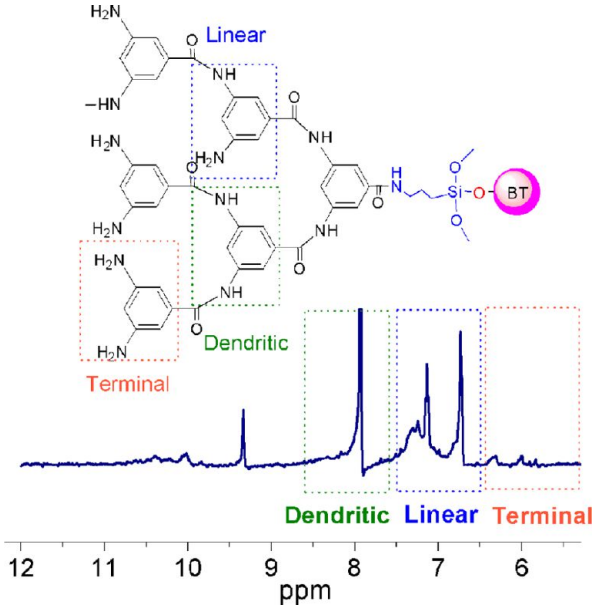

Figure 2. ^{1}H NMR spectra of BT-HBP.

low because of the low content of HBP in BT-HBP, which is evidenced by the following TGA data and TEM images.

Figure 3 displays the TGA curves of BT, BT-APS and BT-HBP nanoparticles. The hyperbranched aromatic polyamide

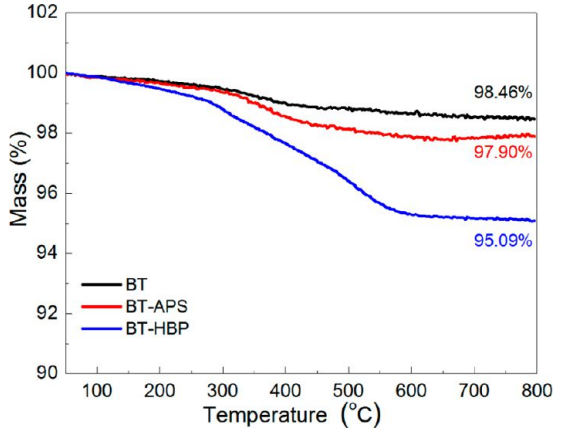

Figure 3. TGA curves for the as-received BT, BT-APS, and BT-HBP.

possesses a lot of intramolecular aromatic structures and can easily be carbonized if it is heated in inert gas, resulting in much residual in the atmosphere of N_2.[28] Therefore, air was chosen as the atmosphere of TGA measurement of BT-HBP. It is can be observed from Figure 3 that the weight loss of the nanoparticles shows the order of BT < BT-APS < BT-HBP at 800 °C. The differences in the TGA data of BT, BT-APS and BT-HBP not only present further evidence to prove the grafting of HBP on the surface of BT, but also give a HBP grafting fraction of about 3 wt % of the BT nanoparticles. If we assume that the density of BT nanoparticles is 6 g/cm^3,[34] the density of HBP layer is 1.35 g/cm^3[28] and the average diameter of BT nanoparticles is 100 nm, then we can estimate that the thickness of the HBP layer on the surface of BT particles is about 3.6 nm, which is similar to that observed from TEM measurements. As shown in Figure 4, all the BT nanoparticles are coated by a polymer layer and its thickness is from several to 5 nm.

dx.doi.org/10.1021/am302959n | ACS Appl. Mater. Interfaces 2013, 5, 1747−1756

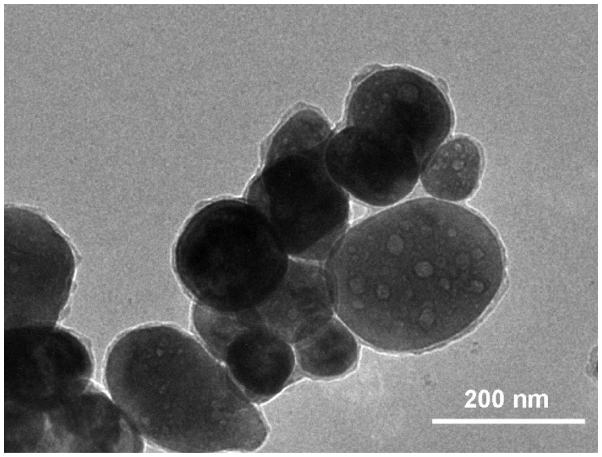

Figure 4. Typical TEM image of the BT-HBP.

Figure 5 displays general XPS spectra of BT-OH, BT-APS and BT-HBP. We can see that the XPS spectra of BT-OH

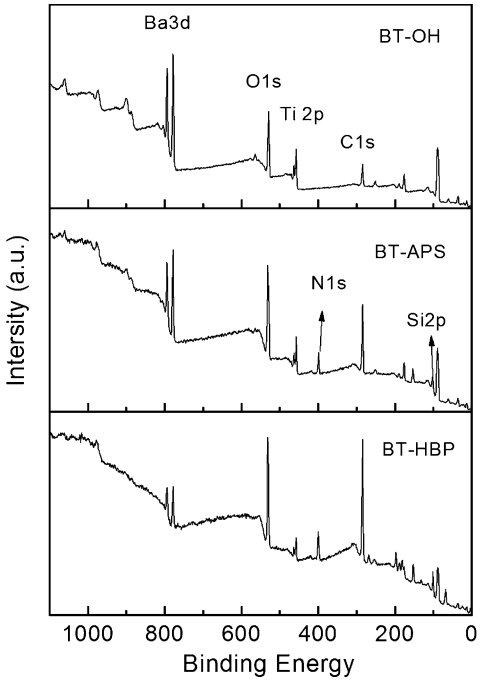

Figure 5. General XPS spectra of BT-OH, BT-APS, and BT-HBP.

shows no peak of N1s and Si2p appearing in the XPS spectra of BT-APS, indicating that APS has been successfully grafted onto the surface of BT-OH. The high-resolution XPS spectra of O1s of BT-OH and BT-APS are shown in Figure 6. In Figure 6a, one can see the peaks of O1s (529.4 and 531.5 eV) corresponding to the O atoms in bulk $BaTiO_3$ and free −OH.[35,36] In Figure 6b, however, a new peak of O1s appears at 532.5 eV, corresponding to −O−Si.[37] The ratio of −OH/−O−Si is about 0.678, indicating that more than half of the free −OH groups reacted with the APS. Figure 7 shows the high-resolution XPS spectra of N1s of BT-OH, BT-APS, and BT-HBP. The peak of N1s in the XPS spectra of BT-OH can hardly be found. After the treatment of BT-OH with APS, the peak of N1s in the XPS spectra of BT-APS appears at 399.0 eV, corresponding to free $-NH_2$. When the hyperbranched polyamide have been grafted onto BT-APS, the peak of N1s becomes wider and shifts to high binding energy, indicating that the free $-NH_2$ are converted to amides (O═C−N, N1s at 400.0 eV).

The particle sizes and their distribution of BT-OH, BT-APS and BT-HBP were measured by dynamic light scattering and the results are shown in Figure 8. It can be found that the size of the particles shows the order of BT-OH < BT-APS < BT-HBP. The difference of sizes indicates that the APS and hyperbranched polyamide have already been grafted successfully onto the surface of BT nanoparticles.

3.2. Microstructure of the BT Nanocomposites. The cylindrical nanocomposite samples were broken in liquid nitrogen and their fracture surfaces were observed by FE-SEM. Figure 9 presents the typical images showing the dispersion of as received-BT and BT-HBP in PVDF-TrFE-CFE. It can be seen from Figure 9 that the BT-HBP nanoparticles slightly aggregate within the matrix, whereas the as-received BT nanoparticles are well-distributed and dispersed. The aggregation of BT-HBP nanoparticles in PVDF-TrFE-CFE is because of the large difference of surface energy between the nanoparticles and the polymer matrix. As explained in the aforementioned content, the as received BT nanoparticles only have a small amount of hydroxyls on their surface, which results in small difference of surface energy between the nanoparticles and polymer matrix and thus good nanoparticle dispersion.

3.3. Dielectric Property of BT-HBP Nanocomposites. Figure 10 shows the frequency-dependent dielectric parameters of PVDF-TrFE-CFE/BT-HBP nanocomposites. The nanocomposites show a significant increase of dielectric constant with the increase of BT-HBP loading. The dielectric constant is ultrahigh at the superlow frequencies and decreases fast as the frequency increases, similar to the dielectric behavior of percolative composites comprising of insulating polymers and conductive fillers.[38,39] Figure 10b displays the frequency-dependent dielectric loss tangent (tan δ) of the BT-HBP nanocomposites. One can see that a relaxation peak appears in the dielectric spectra of the nanocomposites and the peak moves to high frequencies with the increase of nanoparticle loading. The highly filled nanocomposites show excellent dielectric properties at low frequencies. For example, the dielectric constant is higher than 1×10^6 and the dielectric loss tangent is only about 1.3 for the BT-HBP-40 at 1 Hz. Such a dielectric constant value is more than twenty thousand times higher than that of pure polymer (66 at 1 Hz), and ever higher than (or at least comparative with) that of percolative composites.[16,40] Meanwhile, the dielectric loss is only 3.4 times of that of pure polymer. Figure 10c also shows the frequency-dependent electrical conductivity of the nanocomposites. There appears a plateau at low frequency when the volume fraction of BT-HBP is higher than 20%, indicating the existence of conducting network in the BT-HBP nanocomposites.

Because the dielectric constant of the BT-HBP nanocomposites is higher than any of their components, the dielectric enhancement can only be explained by the interfacial polarization, which originates from the charge movement and accumulation at the interface between the fillers and polymer matrix. There are numerous $-NH_2$ groups in the termination of HBP grafted onto the surface of BT nanoparticles, which can cause large difference in conductivity between the surface of BT-HBP and the polymer matrix, resulting in interfacial polarization. Moreover, the $-NH_2$ groups may be partially changed into $-NH_3^+$,[41] resulting in higher electrical con-

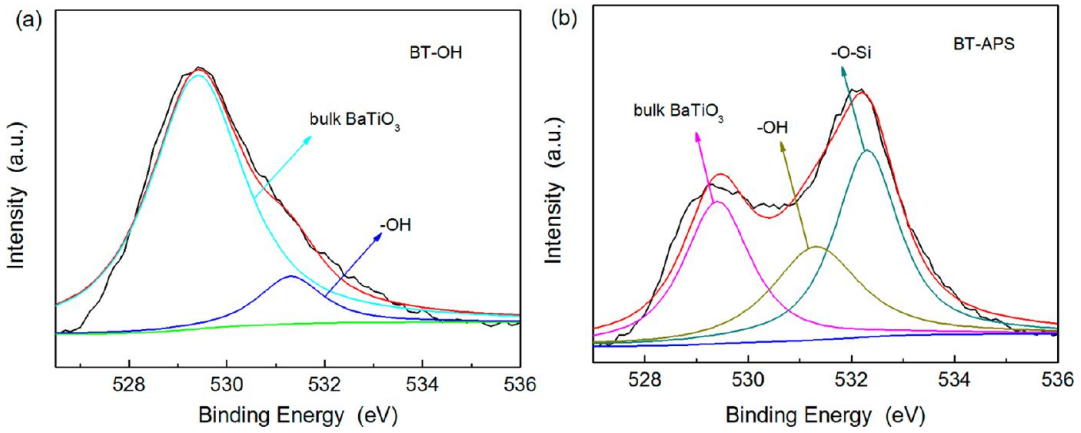

Figure 6. High-resolution XPS spectra of O1s of (a) BT-OH and (b) BT-APS.

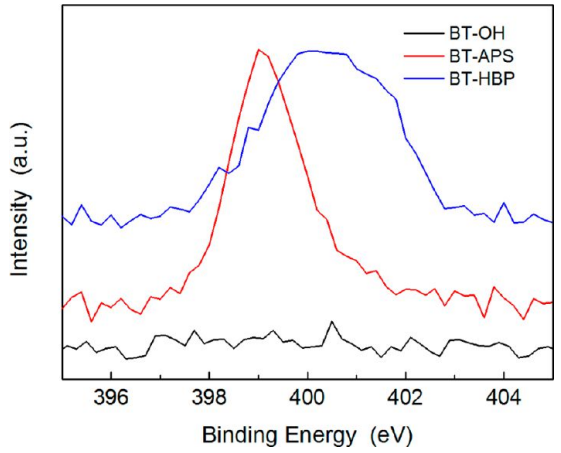

Figure 7. High-resolution XPS spectra of N1s of BT-OH, BT-APS, and BT-HBP.

ductivity on the surface of BT-HBP and thus enhanced interfacial polarization.

Figure 10d displays the dielectric loss factor ε'' of the BT-HBP nanocomposites. We can see that ε'' depends on the frequency largely and decreases as the frequency increases. The loss factor ε'' may be considered as the contribution of three distinct factors: DC conductance, interfacial polarization and the dipole orientation or Debye loss.[6,42−44] Therefore, it can be expressed as following

$$\varepsilon'' = \varepsilon''_{dc} + \varepsilon''_{MW} + \varepsilon''_{D} \quad (1)$$

where ε''_{dc} , ε''_{MW}, and ε''_{D} are due to dc conduction, interfacial polarization, and dipole orientation, respectively. The ε''_{dc} and ε''_{MW} are expressed as

$$\varepsilon''_{dc} = \frac{\sigma dc}{2\pi f} \quad (2)$$

and

$$\varepsilon''_{MW} \propto \left(1 + \frac{K}{1 + (2\pi f)^2 \tau^2}\right) \quad (3)$$

respectively. K is related to the dielectric constant of the sample at the interfaces and τ is the relaxation time of the interfacial polarization.

From eq 3 and 4, we can deduce that the loss factors attributed to DC conductance and interfacial polarization versus frequency demonstrate a straight line and a sigmoidal curve on a log-log plot, respectively. According to the Figure 10d, we can see that at low frequencies, the plots of log ε'' versus log f for the pure polymer and the nanocomposites with BT content lower than 20 vol % show a linear relationship, suggesting that the dc conductance process contributes to the loss factor ε" more significantly at low frequency.

It should be noted from Figure 10c that, for the nanocomposites with higher loading of BT-HBP, the ac conductivity of the nanocomposites with 40 vol % BT-HBP shows a steplike increase in low frequencies. This feature indicates there exists electrode polarization at the interface between the electrodes and the sample,[45] which can obscure the loss mechanisms. To ignore the difficulties of electrode nature and contact, the electric modulus formulism was used to

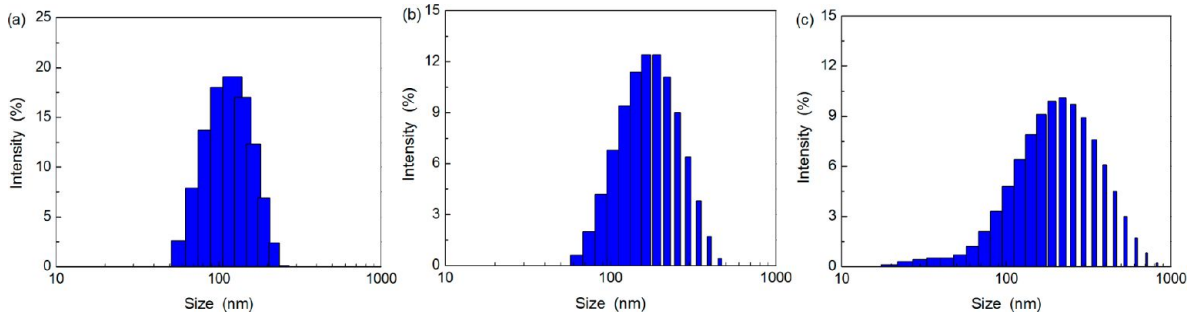

Figure 8. Particle sizes and their distribution of BT-OH, BT-APS, and BT-HBP.

dx.doi.org/10.1021/am302959n | ACS Appl. Mater. Interfaces 2013, 5, 1747−1756

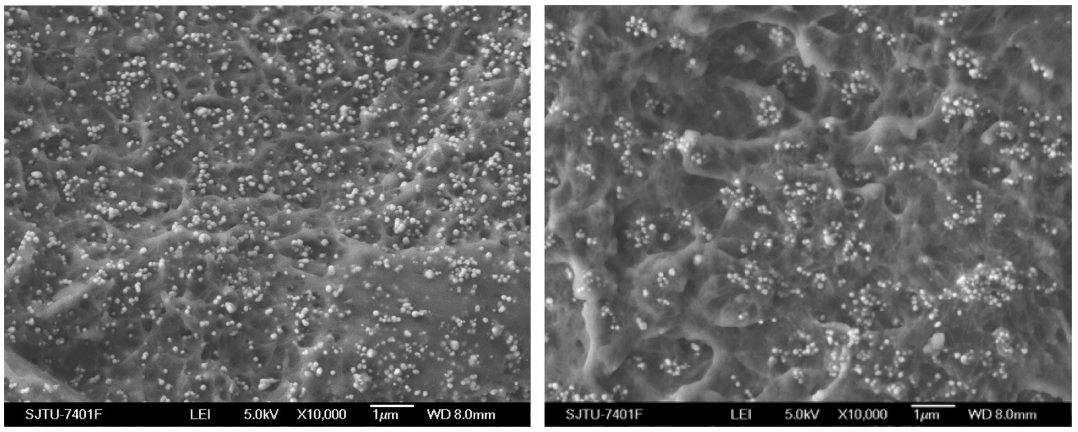

Figure 9. SEM images of the fracture surface of the nanocomposites with as-received BT (left) and BT-HBP (right).

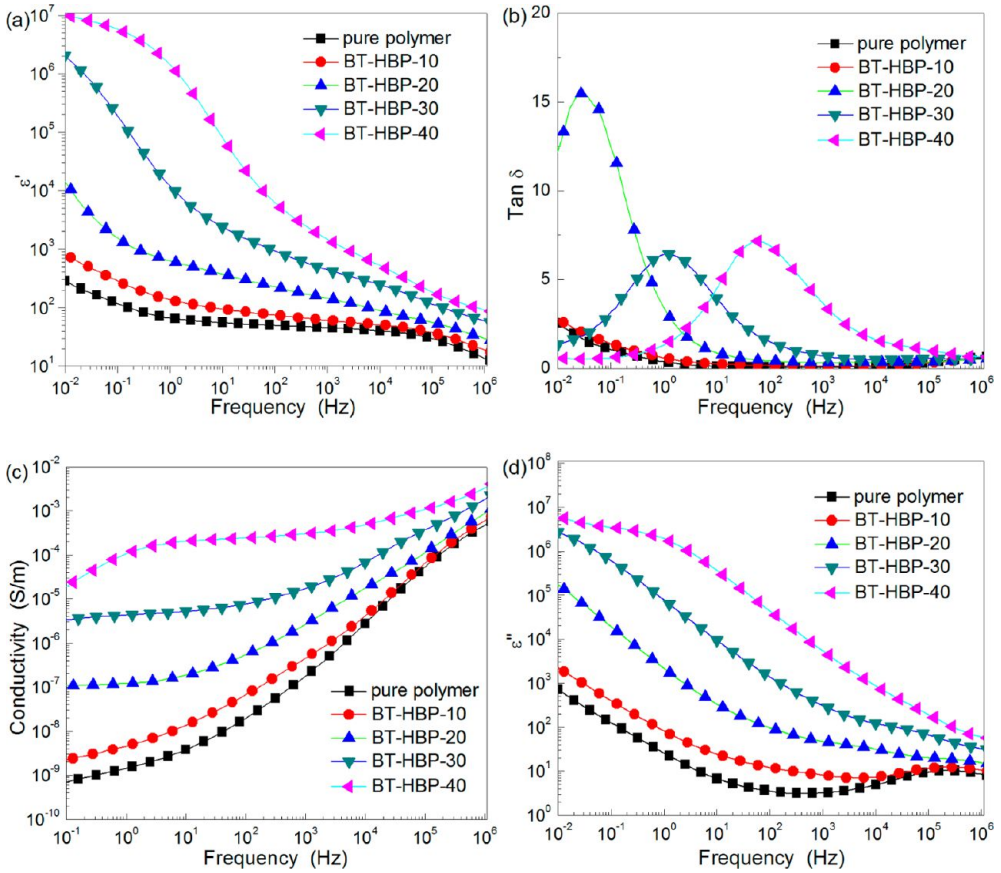

Figure 10. Frequency dependence of (a) dielectric constant, (b) dielectric loss, (c) conductivity, and (d) dielectric loss factor of BT-HBP nanocomposites.

analyze the dielectric data.[46] Electric modulus, M^*, is defined by the following equation

$$M^* = \frac{1}{\varepsilon^*} = \frac{1}{\varepsilon' - j\varepsilon''} = \frac{\varepsilon'}{\varepsilon^{2'} + \varepsilon^{2''}} + j\frac{\varepsilon''}{\varepsilon^{2'} + \varepsilon^{2''}} = M' + j\,M'' \quad (4)$$

Figure 11 displays the dependence of the imaginary part of electric modulus (M'') on the frequency of the BT-HBP nanocomposites. It can be observed from Figure 11 that a relaxation peak associated with interfacial polarization of BT-HBP nanocomposites appears at low frequencies, which should be attributed to the charge accumulation in the interface between BT-HBP and the polymer matrix. The relaxation peak moves to high frequencies with the increase of filler loading. As the BT-HBP nanoparticles loading increases, the conductivity of BT-HBP nanocomposites increases, which can be seen from Figure 10c. The increase in conductivity facilitates the movement and accumulation of free charges, decreasing the time for the free charges to relax. Namely the relaxation peaks shift to higher frequencies. The similar result has been reported in numerous percolative composite systems.[47−49] There also exists an interfacial relaxation peak in the pure polymer at 0.5 Hz, which may originate from the charge accumulation on the

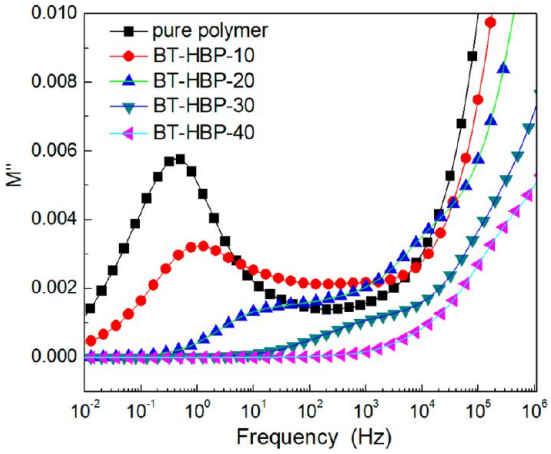

Figure 11. Frequency dependence of the imaginary part of electric modulus of the BT-HBP nanocomposites.

boundary between the lamellar crystal and interlamellar amorphous region.[49]

3.4. Role of BT Functionalization by HBP on Dielectric Property of the Nanocomposites. Figure 12 shows the dielectric constant of the nanocomposite samples with as received BT and BT-HBP at different frequencies. We can see that, compared with the samples with as received BT, the samples with BT-HBP can exhibit much higher dielectric constant at low frequencies. For instance, at a BT-HBP loading of 40 vol %, the 1000 Hz dielectric constant is 1484.5, which is seven times of that (206.3) of the nanocomposites with as-received BT. However, the enhancement of dielectric constant induced by the nanoparticle surface chemistry are closely associated with the electric field frequency and nanoparticle loading: (i) Only at nanoparticle loading higher than 20 vol%, the BT-HBP nanocomposites show enhanced dielectric constant; (ii) At a low nanoparticle loading of 10 vol%, the nanocomposite sample does not show increased dielectric constant at all at the whole frequency range; (iii) at high frequencies (e.g., 1M Hz), the nanocomposite samples with BT-HBP loading higher than 30 vol% show lower dielectric constant in comparison with the nanocomposite samples with as received BT. These results further demonstrated that the dielectric property of the BT-HBP nanocomposites is determined by the interfacial polarization. According to the dielectric measurement result, the electrical conductivity of pure HBP is 2.36×10^{-7} S/m at 100 Hz, which is much higher than that of the BT nanoparticles reported in the literature.[50] Higher surface electrical conductivity of the BT-HBP can cause higher magnitude of interfacial polarization, which in turn results in high dielectric constant at BT-HBP nanocomposites. Interfacial polarization only occurs at low frequencies, and thus the lower dielectric constant of BT-HBP nanocomposites can be explained by the lower dielectric constant of HBP grafted on the surface of BT nanoparticles. As shown in Figure 13, the dielectric constant of pure HBP is only 5.5 at 1 MHz, which is much lower than that of the pure polymer and the BT nanoparticles.[51] At low nanoparticle loading of 10 vol %, the comparative values of dielectric constant in the nanocomposites with as-received BT and BT-HBP nanocomposites might be attributed to the relatively poor dispersion of BT-HBP in the

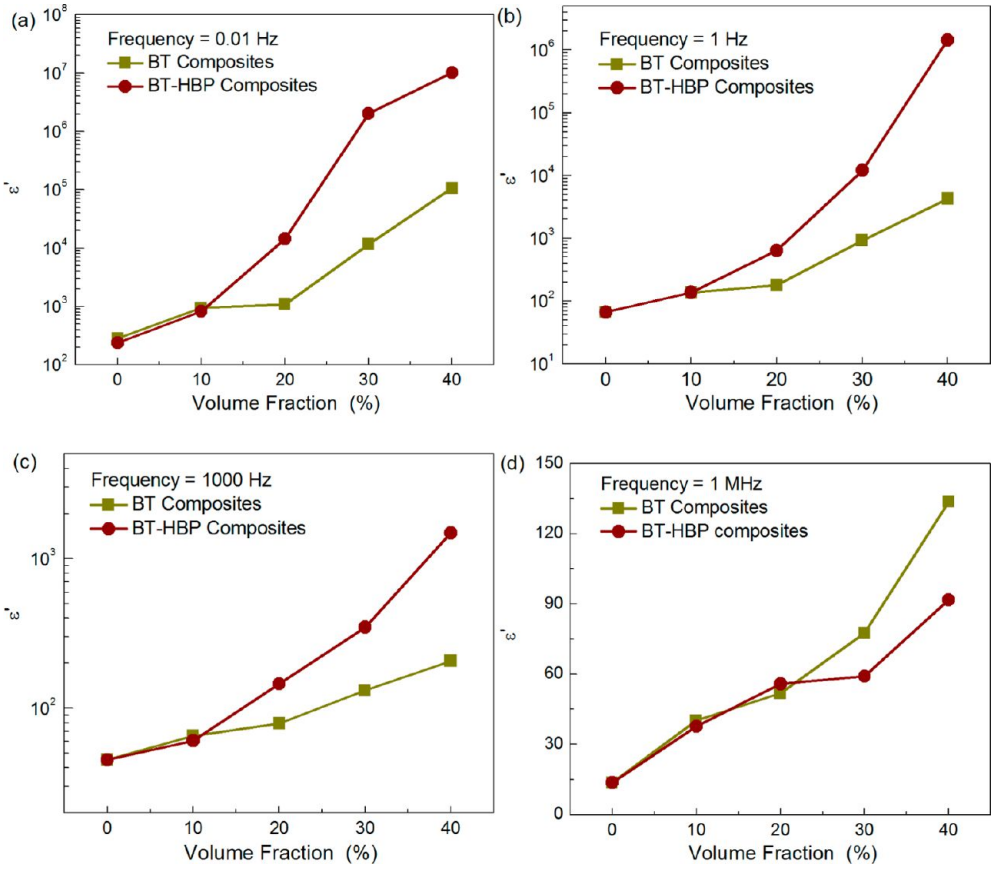

Figure 12. Dielectric constant of BT and BT-HBP nanocomposites at (a) 0.01 Hz, (b) 1 Hz, (c) 1 kHz, and (d) 1 MHz.

dx.doi.org/10.1021/am302959n | ACS Appl. Mater. Interfaces 2013, 5, 1747−1756

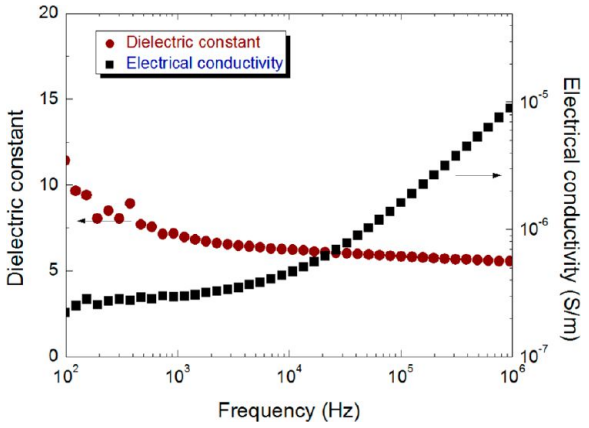

Figure 13. Frequency-dependent dielectric constant and electrical conductivity of hyperbranched aromatic polyamide at room temperature.

polymer matrix (see Figure 9), which results in lower interfacial area and thus weak interfacial polarization in the BT-HBP nanocomposites.

Figure 14 illustrates the temperature-dependent dielectric constant of the nanocomposite with 30 vol % BT-HBP and pure polymer. As showed in Figure 14, a broad dielectric constant peak of pure polymer appears at 25 °C in 1000 Hz spectrum, which is similar to the result reported elsewhere.[47] The peak is due to the kinetics related to the freezing of dipolar motion in the ferroelectric relaxor.[52] The peak shifts to higher temperatures after the addition of BT-HBP nanoparticles, suggesting that the BT-HBP nanoparticles can help to stabilize the polar phase in the pure polymer.[47] Meanwhile, the peak moves to high temperature as the frequency increases. At a low frequency (Figure 14a), the relaxation peak of the pure polymer disappears and the dielectric constant increases with the increase of temperature.

3.5. Electric Breakdown Strength and Maximum Storage Energy Density. The breakdown strength of the BT-HBP nanocomposites was evaluated, and the results were provided in Figure 15. The breakdown strength decreases with

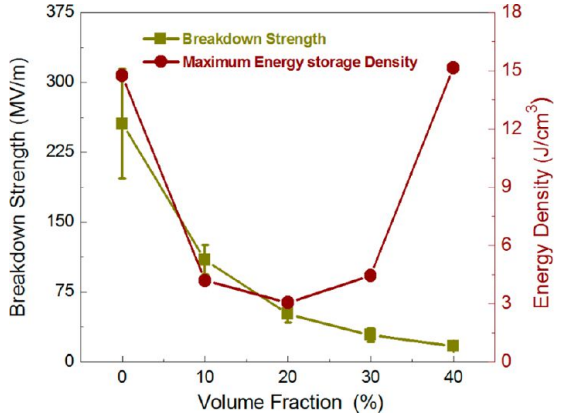

Figure 15. Breakdown strength and the calculated maximum energy storage density of the BT-HBP nanocomposites.

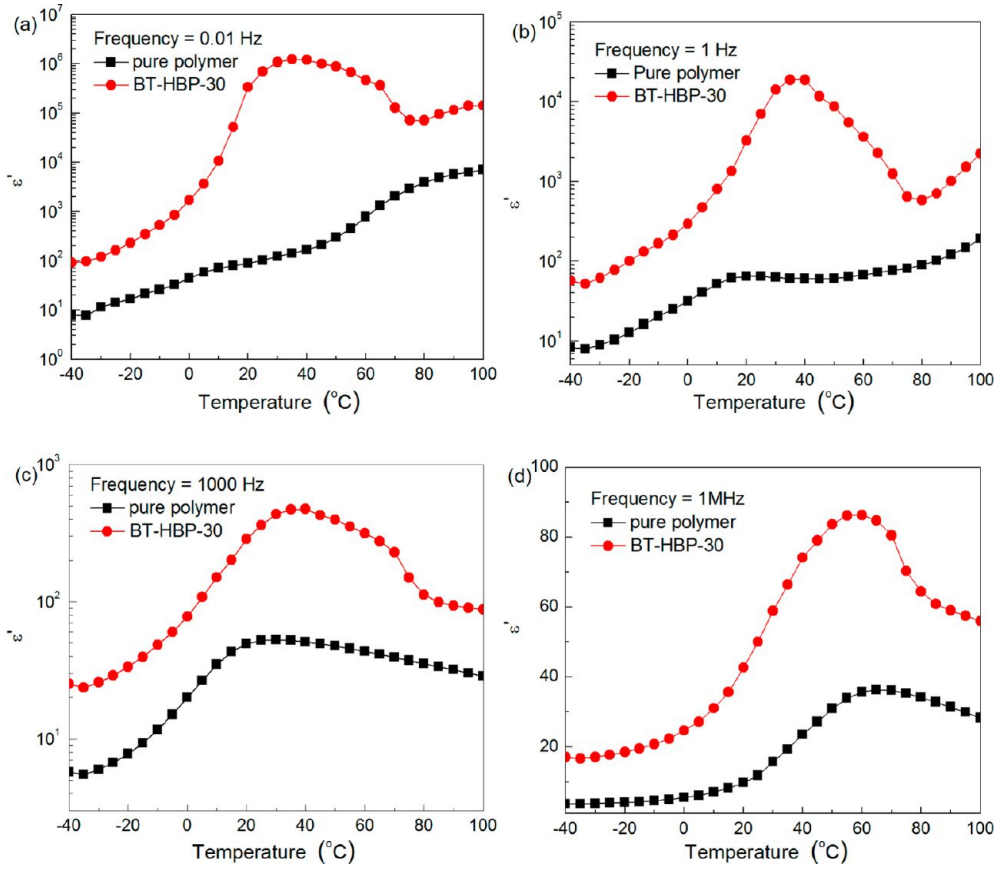

Figure 14. Temperature-dependent dielectric constant of the pure polymer and nanocomposite with 30% BT-HBP at (a) 0.01 Hz, (b) 1 Hz, (c) 1 kHz, and (d) 1 MHz.

dx.doi.org/10.1021/am302959n | ACS Appl. Mater. Interfaces 2013, 5, 1747−1756

the BT-HBP loading, which can be explained by the enhancement of electric field near the interface due to the differences of electric properties between fillers and polymer matrix.[53] However, unlike percolative composites in which the breakdown strength tends to zero near the percolation threshold,[54] the breakdown strength of highly filled BT-HBP nanocomposites can retain a certain value. For example, the breakdown strength is 17.1 MV/m for BT-HBP-40. The retained breakdown strength is important for the practical application. The maximum storage energy densities of BT-HBP nanocomposites were calculated according the following equation[13,55]

$$U = \frac{1}{2}\varepsilon_0 \varepsilon E^2 \tag{5}$$

where ε is the dielectric constant of the composites and E is the breakdown strength. Figure 15 displays the calculated maximum storage energy densities of the BT-HBP nanocomposites at power frequency (50 Hz). As the filler loading increases, the maximum storage energy density firstly decreases and then increases. At the highest loading of BT-HBP (40 vol %), the maximum energy density of the BT-HBP nanocomposites have the same level in comparison with the pure polymer. This result is important for practical application because that the BT-HBP nanocomposites can show high enough storage energy density under a much lower voltage.

4. CONCLUSIONS

A strategy to prepare polymer nanocomposites with the dielectric constant comparable to that of percolative composites has been developed. This method uses core−shell structured hyperbranched aromatic polyamide grafted barium titanate (BT-HBP) as filler and poly (vinylidene fluoride-trifluoroethylene-chlorofluoroethylene) (PVDF-TrFE-CFE) as the polymer matrix. Our results show that the nanocomposites, especially those with high filler loading, have excellent dielectric property. A high dielectric constant of 1485.5 at 1000 Hz is observed for the nanocomposite with 40 vol % $BaTiO_3$−HBP, which is much higher than that (206.3) of the nanocomposite sample with the same content of as received $BaTiO_3$. Unlike the percolative composites, the PVDF-TrFE-CFE/BT-HBP nanocomposites have high enough breakdown strength even at high hybrid filler loading, which result in high enough energy storage density at low voltage. Our results indicate the high dielectric constant PVDF-TrFE-CFE/BT-HBP nanocomposites have promising capability in energy storage application.

AUTHOR INFORMATION

Corresponding Author

*E-mail: xyhuang@sjtu.edu.cn (X.H.); pkjiang@sjtu.edu.cn (P.J.).

Notes

The authors declare no competing financial interest.

ACKNOWLEDGMENTS

The authors gratefully acknowledge supports from the National Natural Science Foundation of China (51107081, 51277117), the Research Fund for the Doctoral Program of Higher Education (Grant 20100073120038, 20120073110031), and the Shanghai Leading Academic Discipline Project (Grant B202).

REFERENCES

(1) Ramesh, S.; Shutzberg, B. A.; Huang, C.; Gao, J.; Giannelis, E. P. *IEEE Trans. Adv. Packag.* **2003**, *26*, 17.
(2) Park, K. I.; Lee, S. Y.; Kim, S.; Chang, J.; Kang, S. J. L.; Lee, K. J. *Electrochem. Solid-State Lett.* **2010**, *13*, G57.
(3) Maliakal, A.; Katz, H.; Cotts, P.; Subramoney, S.; Mirau, P. *J. Am. Chem. Soc* **2005**, *127*, 14655.
(4) Huang, C.; Zhang, Q. M. *Adv. Mater.* **2005**, *17*, 1153.
(5) Molberg, M.; Crespy, D.; Rupper, P.; Nuesch, F.; Manson, J. A. E.; Lowe, C.; Opris, D. M. *Adv. Funct. Mater.* **2010**, *20*, 3280.
(6) Huang, X. Y.; Xie, L. Y.; Jiang, P. K.; Wang, G. L.; Liu, F. *J. Phys. D: Appl. Phys.* **2009**, *42*, 245407.
(7) Wang, Q.; Zhu, L. *J. Polym. Sci., Part B: Polym. Phys.* **2011**, *49*, 1421.
(8) Dang, Z. M.; Yuan, J. K.; Zha, J. W.; Zhou, T.; Li, S. T.; Hu, G. H. *Prog. Mater. Sci.* **2012**, *57*, 660.
(9) Chon, J.; Ye, S.; Cha, K. J.; Lee, S. C.; Koo, Y. S.; Jung, J. H.; Kwon, Y. K. *Chem. Mater.* **2010**, *22*, 5445.
(10) Jung, H. M.; Kang, J. H.; Yang, S. Y.; Won, J. C.; Kim, Y. S. *Chem. Mater.* **2010**, *22*, 450.
(11) Stefanescu, E. A.; Tan, X. L.; Lin, Z. Q.; Bowler, N.; Kessler, M. R. *Polymer* **2011**, *52*, 2016.
(12) Guo, N.; DiBenedetto, S. A.; Tewari, P.; Lanagan, M. T.; Ratner, M. A.; Marks, T. J. *Chem. Mater.* **2010**, *22*, 1567.
(13) Kim, P.; Doss, N. M.; Tillotson, J. P.; Hotchkiss, P. J.; Pan, M. J.; Marder, S. R.; Li, J. Y.; Calame, J. P.; Perry, J. W. *ACS Nano* **2009**, *3*, 2581.
(14) Shen, Y.; Lin, Y. H.; Li, M.; Nan, C. W. *Adv. Mater.* **2007**, *19*, 1418.
(15) Huang, X. Y.; Jiang, P. K.; Xie, L. Y. *Appl. Phys. Lett.* **2009**, *95*, 242901.
(16) Potschke, P.; Dudkin, S. M.; Alig, I. *Polymer* **2003**, *44*, 5023.
(17) Kohlmeyer, R. R.; Javadi, A.; Pradhan, B.; Pilla, S.; Setyowati, K.; Chen, J.; Gong, S. Q. *J. Phys. Chem. C* **2009**, *113*, 17626.
(18) Yu, J. H.; Huang, X. Y.; Wu, C.; Jiang, P. K. *IEEE Trans. Dielectr. Electr. Insul.* **2011**, *18*, 478.
(19) Javadi, A.; Xiao, Y. L.; Xu, W. J.; Gong, S. Q. *J. Mater. Chem.* **2012**, *22*, 830.
(20) Dimiev, A.; Lu, W.; Zeller, K.; Crowgey, B.; Kempel, L. C.; Tour, J. M. *ACS Appl. Mater. Interfaces* **2011**, *3*, 4657.
(21) Wu, W.; Huang, X.; Li, S. T.; Jiang, P.; Tanaka, T. *J. Phys. Chem. C* **2012**, *116*, 24887.
(22) Huang, C.; Zhang, Q. M.; Su, J. *Appl. Phys. Lett.* **2003**, *82*, 3502.
(23) Lu, J. X.; Moon, K. S.; Kim, B. K.; Wong, C. P. *Polymer* **2007**, *48*, 1510.
(24) Nan, C. W.; Shen, Y.; Ma, J. In *Annu. Rev. Mater. Res.* **2010**; Vol. *40*, p 131.
(25) Panda, M.; Srinivas, V.; Thakur, A. K. *Appl. Phys. Lett.* **2008**, *93*, 242908.
(26) Almadhoun, M. N.; Bhansali, U. S.; Alshareef, H. N. *J. Mater. Chem.* **2012**, *22*, 11196.
(27) Chang, S. J.; Liao, W. S.; Ciou, C. J.; Lee, J. T.; Li, C. C. *J. Colloid Interface Sci.* **2009**, *329*, 300.
(28) Yu, Y.; Rong, M. Z.; Zhang, M. Q. *Polymer* **2010**, *51*, 492.
(29) Feng, Q. P.; Xie, X. M.; Liu, Y. T.; Zhao, W.; Gao, Y. F. *J. Appl. Polym. Sci.* **2007**, *106*, 2413.
(30) Yu, J. H.; Huang, X. Y.; Wu, C.; Wu, X. F.; Wang, G. L.; Jiang, P. K. *Polymer* **2012**, *53*, 471.
(31) Jikei, M.; Kakimoto, M. A. *J. Polym. Sci., Part A: Polym. Chem.* **2004**, *42*, 1293.
(32) Zhao, J.; Xu, H. J.; Fang, J. H.; Yin, J. *J. Appl. Polym. Sci.* **2012**, *126*, 244.
(33) Yu, J. H.; Huang, X. Y.; Wang, L. C.; Peng, P.; Wu, C.; Wu, X. F.; Jiang, P. K. *Polym. Chem.* **2011**, *2*, 1380.
(34) Agoudjil, B.; Ibos, L.; Candau, Y.; Majeste, J. C. *J. Phys. D: Appl. Phys.* **2008**, *41*, 055407.
(35) Wegmann, M.; Watson, L.; Hendry, A. *J. Am. Ceram. Soc.* **2004**, *87*, 371.

(36) Li, C. C.; Chang, S. J.; Lee, J. T.; Liao, W. S. *Colloids Surf. A* **2010**, *361*, 143.
(37) Xiao, S. J.; Textor, M.; Spencer, N. D.; Wieland, M.; Keller, B.; Sigrist, H. *J. Mater. Sci. Mater. Med.* **1997**, *8*, 867.
(38) Dang, Z. M.; Wang, L.; Yin, Y.; Zhang, Q.; Lei, Q. Q. *Adv. Mater.* **2007**, *19*, 852.
(39) He, F.; Lau, S.; Chan, H. L.; Fan, J. T. *Adv. Mater.* **2009**, *21*, 710.
(40) Yuan, J. K.; Yao, S. H.; Dang, Z. M.; Sylvestre, A.; Genestoux, M.; Bai, J. B. *J. Phys. Chem. C* **2011**, *115*, 5515.
(41) Lin, M. F.; Thakur, V. K.; Tan, E. J.; Lee, P. S. *RSC Adv.* **2011**, *1*, 576.
(42) Stefanescu, E. A.; Tan, X. L.; Lin, Z. Q.; Bowler, N.; Kessler, M. R. *Polymer* **2010**, *51*, 5823.
(43) Jonscher, A. *Nature* **1977**, *267*, 673.
(44) Huang, X.Y.; Zhi, C. Y.; Jiang, P. K.; Golberg, D.; Bando, Y.; Tanaka, T. *Nanotechnology* **2012**, *23*, 455705.
(45) Wang, C. C.; Song, J. F.; Bao, H. M.; Shen, Q. D.; Yang, C. Z. *Adv. Funct. Mater.* **2008**, *18*, 1299.
(46) Soares, B. G.; Leyva, M. E.; Barra, G. M. O.; Khastgir, D. *Eur. Polym. J.* **2006**, *42*, 676.
(47) Li, J. J.; Seok, S. I.; Chu, B. J.; Dogan, F.; Zhang, Q. M.; Wang, Q. *Adv. Mater.* **2009**, *21*, 217.
(48) Wu, C.; Huang, X. Y.; Xie, L. Y.; Yu, J. H.; Jiang, P. K. *J. Mater. Chem.* **2011**, *21*, 17729.
(49) Li, Y.; Huang, X. Y.; Hu, Z. W.; Jiang, P. K.; Li, S. T.; Tanaka, T. *ACS Appl. Mater. Interfaces* **2011**, *3*, 4396.
(50) Hemeda, O. M.; Tawfik, A.; Sharif, A. A.; Amer, M. A.; Kamal, B. M.; El Refaay, D. E.; Bououdina, M. *J. Magn. Magn. Mater.* **2012**, *324*, 4118.
(51) Petrovic, M. M. V.; Bobic, J. D.; Radojkovic, A. M.; Banys, J.; Stojanovic, B. D. *Ceram. Int.* **2012**, *38*, 5347.
(52) Pirc, R.; Blinc, R.; Kutnjak, Z. *Phys. Rev. B: Condens. Matter* **2002**, *65*, 214101.
(53) Flandin, L.; Vouyovitch, L.; Beroual, A.; Bessede, J. L.; D Alberolal, N. *J. Phys. D: Appl. Phys.* **2005**, *38*, 144.
(54) Huang, C.; Zhang, Q. M. *Adv. Funct. Mater.* **2004**, *14*, 501.
(55) Fillery, S. P.; Koerner, H.; Drummy, L.; Dunkerley, E.; Durstock, M. F.; Schmidt, D. F.; Vaia, R. A. *ACS Appl. Mater. Interfaces* **2012**, *4*, 1388.